Earth's Infrared Background

Ofer Shamir[1] and Edwin P. Gerber[1]

[1]Courant Institute of Mathematical Sciences, New York University, New York 10012, New York.

Key Points:

- The Earth's Infrared Background (EIB) is identified as isotropic variability implied by the fluctuation–dissipation theorem.
- The EIB is modeled using a stochastically forced energy balance climate model, yielding a red background consistent with observations.
- The EIB provides a null hypothesis for separating atmospheric signals from natural variability in Outgoing Longwave Radiation.

Corresponding author: Ofer Shamir, `ofer.shamir@courant.nyu.edu`

Abstract

Much of the Outgoing Longwave Radiation (OLR) emitted to space is best described as random variability, or the "Earth's Infrared Background". A rigorous characterization of this background provides an objective null hypothesis and enables the isolation of atmospheric phenomena — such as waves, storms, and other coherent structures — within OLR observations. To this end, we identify the background as isotropic fluctuations implied by the fluctuation–dissipation theorem in response to internal atmospheric variability on small spatiotemporal scales. We use a stochastically forced energy balance climate model, which has a broad sense red spectrum consistent with observations, a first-order process in time, and a second-order process in space. By fitting the model to OLR data from satellite observations, we find that the background fluctuations have an upper bound of about 400 km and 2.5 days on their spatiotemporal (de)correlations, between meso-scale and synoptic-scale weather.

Plain Language Summary

The infrared radiation emitted by Earth carries the "footprints" of weather and climate-related phenomena, imprinted by greenhouse gases and clouds as they interact with the radiation on its way through the atmosphere. At the same time, because of the chaotic/turbulent nature of the atmosphere, the emitted radiation also carries essentially random signals, which make up the Earth's Infrared Background. In order to accurately trace the footprints, one must also isolate the background. To this end, we follow the fluctuation–dissipation principle, according to which the random noise in a system is directly linked to how strongly the system resists disturbances. This allows us to build an empirically consistent model of the background.

1 Introduction

Only a small fraction of the Outgoing Longwave Radiation (OLR) emitted to space, about 17% (about 40 out of 240 $\mathrm{W\,m^{-2}}$, Trenberth et al., 2009; Loeb et al., 2009), originates directly at the surface. The remaining 83% only make it out to space after having been absorbed and re-emitted by greenhouse gases (about 70% of the total OLR, or 170 $\mathrm{W\,m^{-2}}$) and clouds (about 13%, or 30 $\mathrm{W\,m^{-2}}$). Therefore, in addition to its role in determining the global energy budget, OLR also contains the "footprints" of atmospheric variability. On subannual time scales (Fig. 1), for example, OLR exhibits enhanced variability (compared to the global mean STD of 26.5 $\mathrm{W\,m^{-2}}$) over the Intertropical Convergence Zone (Schneider et al., 2014; Liu et al., 2020), monsoonal regions, the Indian Ocean and the Maritime Continent, associated with the Madden–Julian oscillation (Knutson et al., 1986; Weickmann & Khalsa, 1990; M. C. Wheeler & Hendon, 2004; Zhang, 2005; Jiang et al., 2020), and the mid-latitude warm conveyor belts (Shaw et al., 2016). It also exhibits suppressed variability in the polar regions and in regions associated with the El Niño-Southern Oscillation (Philander, 1983; Ardanuy & Kyle, 1986; Chelliah & Arkin, 1992; Chiodi & Harrison, 2013; Timmermann et al., 2018; Fajary et al., 2019). At the same time, much of the observed OLR is best described as random variability, which we term Earth's Infrared Background (EIB). Therefore, to use these footprints quantitatively, it is important to provide a rigorous description of the background so that an objective null hypothesis can be established.

This issue is typically encountered in the Tropics, where the identification of the Tropical OLR background, is essential for the quantitative analysis of equatorial waves and related coherent features (Knippertz et al., 2022). However, despite its importance, a consensual definition is still lacking (Masunaga et al., 2006; Hendon & Wheeler, 2008; Gehne & Kleeman, 2012; Kikuchi, 2014; Marques & Castanheira, 2018; Kikuchi et al., 2018), with existing studies using varying approaches to estimate the background. Perhaps the most prevalent approach consists of successive smoothing (M. Wheeler & Ki-

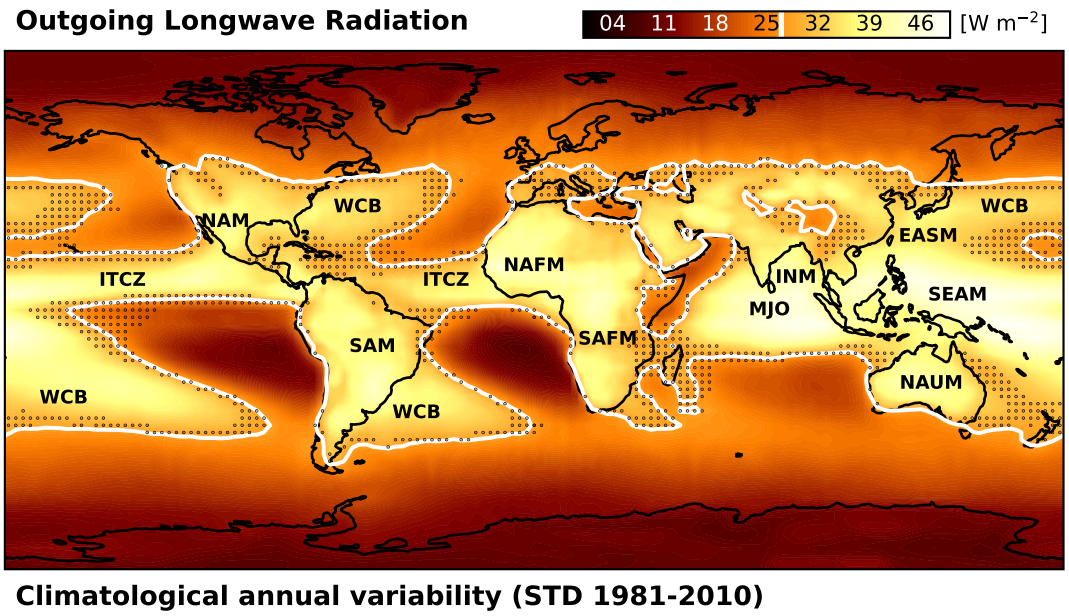

Figure 1. Outgoing Longwave Radiation (OLR). Climatological OLR variability (STD) from satellite observations during the penultimate standard climate normal (1 January, 1981 to 31 December, 2010). The global mean STD (26.5 W m^{-2}) is marked by the white contour and the vertical white line in the colorbar. Stippling indicate points where the observed variance is insignificantly different from a random realization of the background (see Supporting Information S1 for further details on the data, random realizations, and statistical analysis). Marked on the figure are regions of abnormally high variability, compared to the global mean STD, including: The Intertropical Convergence Zone (ITCZ), the Warm Conveyor Belts (WCB), the Madden–Julian oscillation (MJO), and the North American (NAM), South American (SAM), North African (NAFM), South African (SAFM), Indian (INM), East Asian (EASM), South Asian (SEAM), and North Australian (NAUM) Monsoons.

ladis, 1999), which gradually redistributes the power in spectral space towards a uniform distribution, i.e. leading to an asymptotically white background. Alternatively, based on the observation that the OLR has a broad red background, in the sense that its power decays with decreasing spatiotemporal scales, some studies assume a priori that the background follows a red-noise process (Masunaga et al., 2006; Hendon & Wheeler, 2008; Kikuchi, 2014; Marques & Castanheira, 2018), albeit only in time. The most relevant approach in the present context is that of stochastic modeling pioneered by Hottovy and Stechmann (2015), where the background is modeled as the response to a white noise forcing, representing turbulent eddy fluxes. Standard results in stochastic climate modeling (Hasselmann, 1976; North et al., 2011) confirm that the resulting background in this approach is indeed broad sense red, a first-order process in time and second-order in space.

In this work, we consider a global OLR background on subannual time scales, and identify it with isotropic variability implied by the fluctuation-dissipation theorem (FDT, Kubo, 1966) in response to the internal variability of the atmosphere. The underlying idea is that, under weak perturbations, the noise level of the system is determined by its dissipative properties and equilibrium distribution. Like classical Brownian motion, we assume a scale separation between the response and the forcing, such that the latter can be approximated as a white noise process. Unlike classical Brownian motion, however, the equilibrium distribution is not derived from first principles and is only estimated empirically. In addition, the dissipation is modeled using the "simplest" mathematical terms (Section 2), and the associated coefficients are also estimated empirically to fit observations. Although the resulting background is empirical, it meets our aim of providing an objective and quantitative null hypothesis for isolating atmospheric variability on subannual time scales. In addition, while implying the use of a stochastic model similar to that of Hottovy and Stechmann (2015), the present approach places an additional constraint on the power spectrum of the forcing.

The assumption that the background is statistically isotropic is the spherical equivalent of statistical homogeneity in time series analysis and provides the most conservative null hypothesis for the variance. This amounts to the assumption that any anisotropy observed in the data reflects genuine physical variability rather than an artifact of the noise. We stress that the observed OLR is far from isotropic, as evident by its non-uniform variance in Fig. 1 (a necessary condition for statistical isotropy). However, the identified regions of enhanced/suppressed variability in Fig.1 are associated with non-equilibrium phenomena and are the very things the null hypothesis is designed to detect.

2 A Stochastically Forced Energy Balance Climate Model ($\mathcal{E}$BCM)

A quantitative description of the background, and the associated foreground, requires an empirically consistent model. The most parsimonious, lowest order, model of isotropic fluctuations that captures the above physical picture and the observed OLR variance on subannual time scales is given by the following stochastic differential equation:

$$\tau_0 \frac{\partial F}{\partial t} - \lambda_0^2 \nabla^2 F + F = S. \tag{1}$$

Here F represents OLR fluctuations, and S represents a stochastic forcing due to internal fluctuations of the atmosphere. The model has a total of 3 free parameters, a time scale τ_0, which sets the temporal decorrelation, a length scale λ_0, which sets the spatial decorrelation, and an amplitude ϵ_0, which sets the variance and enters through the forcing S as described below.

This model has been extensively analyzed in the context of energy balance climate models ($\mathcal{E}$BCMs, North, 1975; North et al., 1981), where some of its applications include the study of second-order surface temperature statistics (Kim & North, 1991; North et al., 2011), and climate predictability bounds (North & Cahalan, 1981). Save for the scale-dependence of the forcing, described below, the present analysis follows these works. How-

ever, while resulting in a similar model, our reasoning is different. In particular, we have no reason to assume that purely random OLR fluctuations are subject to Fickian diffusion. Rather, in the present context, the Laplacian on the left-hand side is the lowest order differential operator (other than the identity) that is invariant under rotation, which guarantees that the response to a statistically isotropic forcing remains isotropic (North & Cahalan, 1981; North et al., 2011), while the relaxation term guarantees that the response remains statistically stationary (Hasselmann, 1976; Frankignoul & Hasselmann, 1977). A complementary viewpoint is provided in Hottovy and Stechmann (2015), who studied a similar model in the context of the tropical background, and suggested that it represents the effects of mean and eddy flux convergence in a turbulent atmosphere.

We take the forcing to be Gaussian white noise in time and statistically isotropic in space. The former implies that the forcing is delta correlated in time, assuming a priori that the forcing decorrelates much faster than the response. The latter implies that the forcing is delta correlated in Spherical Harmonics space, and depends at most on the multiple moment (Obukhov, 1947), i.e.,

$$\langle S_{lm}(t) S^*_{l'm'}(t') \rangle = 2\epsilon_0^2 \tau_l \delta_{ll'} \delta_{mm'} \delta(t - t'), \tag{2}$$

where S_{lm} are the spectral coefficients of S, asterisks denote complex conjugates, angle brackets denote ensemble averages, sub-scripted δ_{ij} is the Kronecker delta, and argumented $\delta()$ is the Dirac delta. In a key departure from earlier works (North et al., 2011; Hottovy & Stechmann, 2015), we find it necessary to allow the forcing to be scale dependent (l dependent) to explain the observed OLR. Here $\tau_l = \tau_0/[1+\lambda_0^2 l(l+1)/a^2]$, where a is the mean radius of the Earth, which is the only choice consistent with the FDT (Supporting Information S2). We note that the spatial decorrelation of the forcing is much faster than that of the resulting response (Supporting Information S3), so that the two are well separated in both space and time.

The process in Eq. (1) is fully determined by its covariance function, which for an isotropic process depends only on the scale l and is termed angular covariance. The asymp-

totic angular covariance, at times much greater than the decorrelation time ($t, t' \gg \tau_l$), is (e.g., Zwanzig, 2001, see also Supporting Information S2):

$$C_l(t,t') = \langle F_{lm}(t) F^*_{lm}(t') \rangle = \epsilon_l^2 e^{-|t-t'|/\tau_l}, \tag{3}$$

where F_{lm} are the spectral coefficients of F and $\epsilon_l = \epsilon_0 \tau_l / \tau_0$. For the background spectrum, we will use the corresponding power spectral density (PSD):

$$\hat{C}_l(\omega) = 2\epsilon_l^2 \tau_l / \left[\omega^2 \tau_l^2 + 1\right], \tag{4}$$

where hats denote the Fourier modes in frequency domain, obtained from the covariance via the Wiener–Khinchin theorem, i.e., $\hat{C}_l(\omega) = \int_{-\infty}^{\infty} C_l(\tau) e^{-i\omega\tau} d\tau$.

3 Estimating the model parameters from observations

Before turning to estimating the background and associated foreground, we use Eqs. (3) and (4) to estimate ϵ_0, λ_0, and τ_0 from observations (Supporting Information S1) and discuss their physical meaning.

Consider first the angular power spectrum of the EIB (Fig. 2), obtained by multiplying the time-dependent Spherical Harmonics coefficient by their complex conjugates $F_{lm}(t)F^*_{lm}(t)$ and averaging over time and m (with $|m| \leq l$) to estimate the angular variance $C_l = \langle F_{lm} F^*_{lm} \rangle$. By the Wiener-Khinchin theorem, the latter is related to the PSD via $C_l(t = t') = \int_{-\infty}^{\infty} \hat{C}_l(\omega) d\omega \,/2\pi$, and therefore provides a measure of the angular power spectrum in terms of the frequency-averaged PSD. At small spatial scales (large l), the $\mathcal{E}$BCM (black line) can accurately fit the raw variance (orange) by setting $t = t'$ in Eq. (3) and using non-linear least squares to estimate $\epsilon_0 = 5.8 \pm 0.1$ W m^{-2} and $\lambda_0 = 384 \pm 2$ km. At large spatial scales (small l), however, there are externally forced variations and the $\mathcal{E}$BCM can only explain the observed variance on subannual time scales with frequencies above 1/360 cpd (blue). The peak at $l = 15$ is an artifact corresponding to the satellite swath half-width of about 1,250 km. A weaker imprint of the satellite swath width is also found at $l = 13$ (Supporting Information S3).

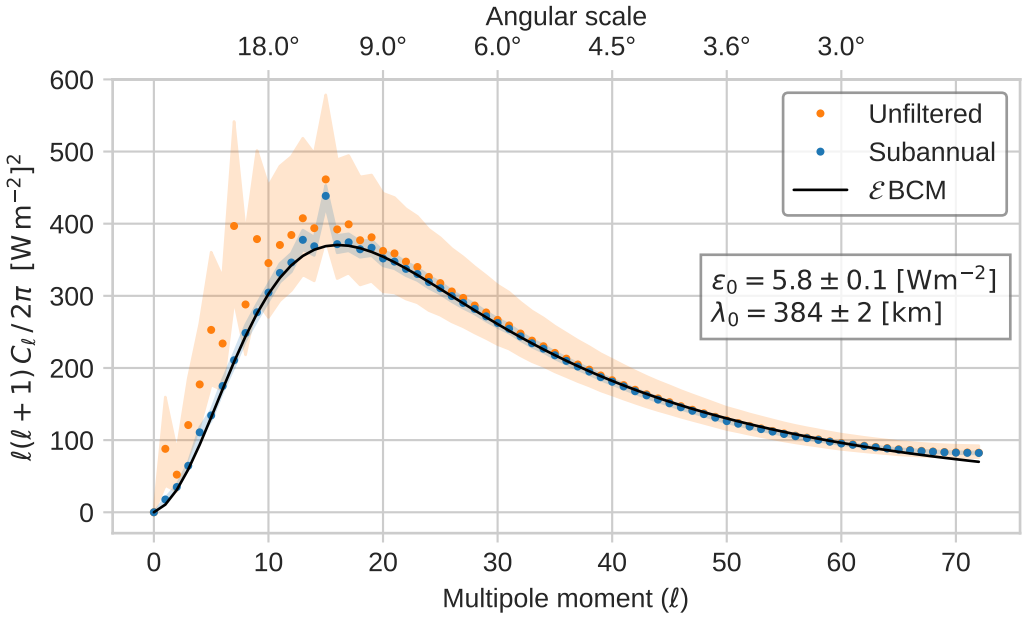

Figure 2. The Angular power spectrum is obtained by averaging OLR fluctuations in spectral space, $F_{lm}(t)F^*_{lm}(t)$, over time and m (with $|m| \leq l$) to estimate the angular variance $C_l = \langle F_{lm}F^*_{lm}\rangle$ (orange). The angular variance provided by the $\mathcal{E}$BCM (Eq. 3 with $t = t'$, black line) is fit to the data on subannual time scales (including frequencies above 1/360 cpd, blue) using nonlinear least squares to estimate ϵ_0 and λ_0. With the scaling on the ordinate, the figure represent the power per logarithmic interval in angular scale. The peak at $l = 15$ (12°) is an artifact corresponding to the satellite swath half-width of about 1,250 km. The uncertainty in the raw data is associated with the variance across m, while the uncertainty in the subseasonal data is associated with the variance across both m and the temporal windows (see Supporting Information S3).

In the context of the stochastic model used here, λ_0 determines the spatial decorrelation of the EIB. More precisely, λ_0 provides an upper bound on the spatial decorrelation. The effective decorrelation decreases with increasing frequency (Supporting Information S3) and is not simply an e-folding scale (North et al., 2011). The estimated value of $\lambda_0 = 384 \pm 2$ km is well below the Nyquist wavelength of 5° in the data, consistent with random fluctuations with spatial decorrelation smaller than the smallest resolvable waves. In addition, λ_0 is also smaller than the typical Rossby deformation radius, providing further reassurance that the background is associated with random fluctuations and suggesting that it is constrained by linear wave dynamics.

Next, consider the temporal power spectrum (Fig. 3), obtained by applying a discrete Fourier transform on the time-dependent Spherical Harmonics coefficient to estimate the PSD $\tilde{F}_{lm}(\omega)\tilde{F}^*_{lm}(\omega)/\Delta\omega$, where $\Delta\omega$ is the frequency resolution, and averaging over m (with $|m| \leq l$) and l. The uptick at $\omega = 1$ cpd (the Nyquist frequency) results from stratospheric tides associated with the diurnal cycle, as well as aliasing by higher frequency gravity waves. The uptick at $\omega = 0.9$ cpd (a period of 1.1 day) is associated with the satellite orbit (M. Wheeler & Kiladis, 1999), and the upward inflection at $\omega >$ 0.6 cpd is the result of spectral leakage (Supporting Information S1). The dominant harmonics at $(1, 2, 3, 4)/365$ cpd (vertical dashed lines) correspond to the annual, semi-annual, and seasonal cycles, and were explicitly removed before fitting the model (Supporting Information S1). Having estimated ϵ_0 and λ_0 from the angular power spectrum, τ_0 can now be estimated by averaging Eq. (4) over l and using non-linear least squares (black line), yielding $\tau_0 = 2.3 \pm 0.1$ days. Consistent with the angular variance in Fig. 2, it is also evident in this figure that the $\mathcal{E}$BCM fits the temporal power spectrum only on sub-annual time scales with frequencies above 1/360 cpd.

In the context of the stochastic model used here, τ_0 provides an upper bound on the temporal decorrelation, which has an l-dependent e-folding scale $\tau_l = \tau_0/[1+\lambda_0^2 l(l+1)/a^2]$, as implied by Eq. (3). At $l = 0$, the temporal decorrelation is at the lower limit

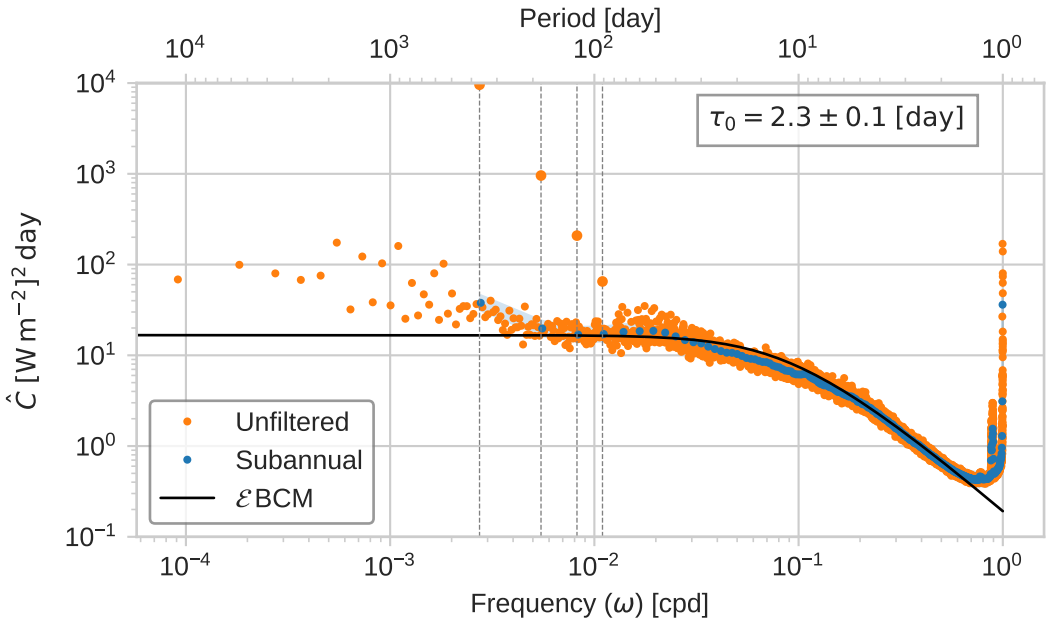

Figure 3. The temporal power spectrum is obtained by applying a discrete Fourier transform to the time-dependent Spherical Harmonics coefficient to estimate the PSD $\tilde{F}_{lm}(\omega)\tilde{F}^*_{lm}(\omega)/\Delta\omega$, where $\Delta\omega$ is the frequency resolution, and averaging over m (with $|m| \leq l$) and l (orange). The PSD provided by the $\mathcal{E}$BCM (Eq. 4, black line) averaged over l is fit to the data on subannual time scales (including frequencies above 1/360 cpd, blue) using the values of ϵ_0 and λ_0 estimated in Fig. 2, and nonlinear least squares to estimate τ_0. The figure represents the power per frequency. Vertical dashed lines indicate the annual cycle at 1/365 cpd and subsequent three harmonics: $(2, 3, 4)/365$ cpd. The uncertainty in the raw data is associated with the variance across m, while the uncertainty in the subseasonal data is associated with the variance across both m and the temporal windows.

of synoptic-scale weather, typically taken as 2 days. At $l = 20$ (about 1000 km), the decorrelation is 22 hours, at the upper limit of meso-scale weather, typically taken as 1 days and 1000 km. Alternatively, considering also the angular power spectrum, a less arbitrary definition of the transition between synoptic and meso-scale weather might be the inflection point (maximum in Fig. 2) at $l = 16$ (11.25°, about 1250 km), where the temporal decorrelation is 28 hours. If so, the above results imply that the damping mechanism is dominated by linear relaxation at synoptic-scales and diffusion at meso-scales. Finally, at $l = 72$ (about 300 km), the decorrelation is 3 hours, at the lower limit of meso-scale weather. This last value is important since, by assumption, the temporal correlation of the forcing is much shorter than that of the response. Therefore, allowing for sufficient scale separation between the two, the forcing mechanism(s) ought to be sufficiently faster than meso-scale weather.

4 Estimating the background and associated foreground

The full description of the EIB consists of its joint power distribution in ω, l, m space. We consider the PSD obtained by first applying a discrete Fourier transform to the time-dependent Spherical Harmonic coefficients to estimate $\tilde{F}_{lm}(\omega)\tilde{F}^*_{lm}(\omega)/\Delta\omega$, and then averaging over m (with $|m| \leq l$) or l (with $|m| \leq l \leq 72$) to obtain the PSD as a function of ω and l (Fig. 4, top row) or ω and m (Fig. 4, bottom row), respectively. Note that for the latter, the background (Fig. 4E) depends on m implicitly through the m-dependent averaging, although the $\mathcal{E}$BCM does not.

A common source of confusion, particularly in the study of the tropical spectrum, has been the fact that the background has the same amount of total variance as the raw data. The same is also true here. Using the values of ϵ_0 and λ_0 estimated above, the total variance of the $\mathcal{E}$BCM is 8891 ± 314 $[\mathrm{W\,m^{-2}}]^2$, which is in agreement with the observed value of 9113 ± 309 $[\mathrm{W\,m^{-2}}]^2$ (see Supporting Information S1 for the variance calculations). However, the fact that the two have the same amount of total variance does

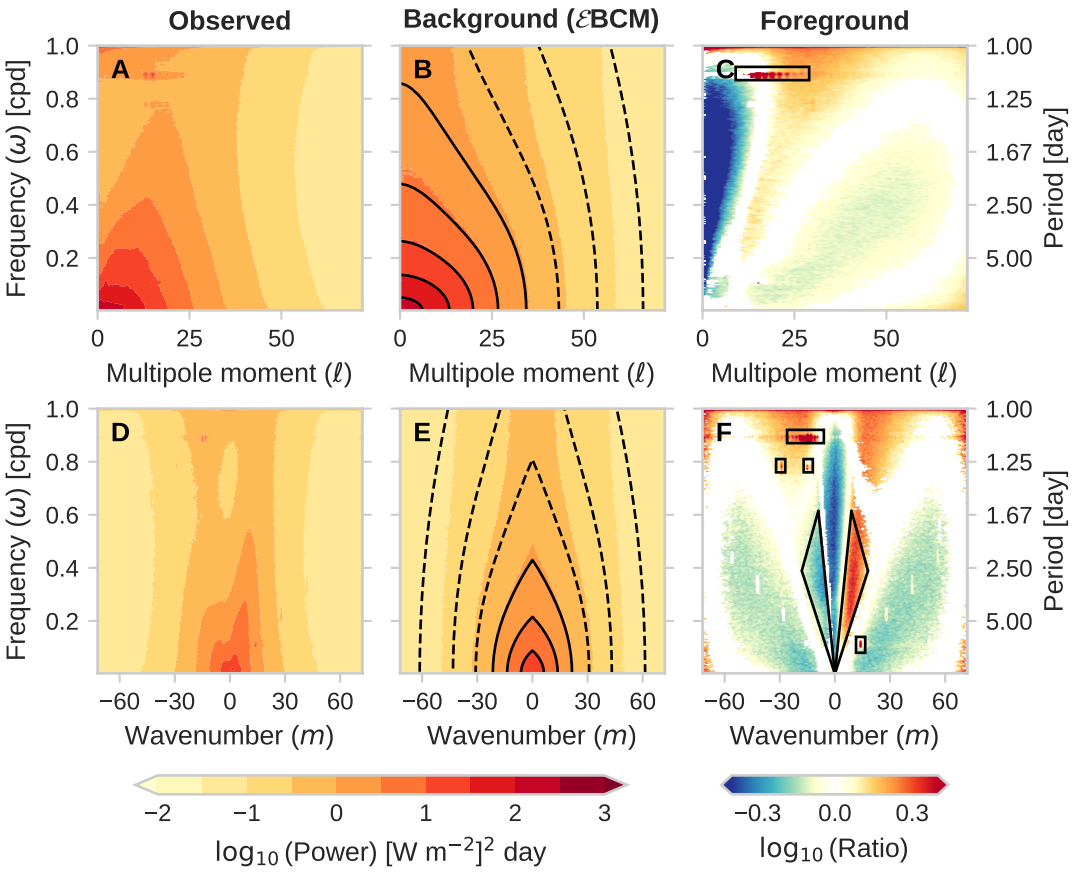

Figure 4. Space-time spectra. The power spectral density (PSD) of the observed OLR are obtained by averaging $\tilde{F}_{lm}(\omega)\tilde{F}^{*}_{lm}(\omega)/\Delta\omega$, where tildes denote the Discrete Fourier Transform and $\Delta\omega$ is the frequency resolution, over zonal wavenumber m (**A**) and total wavenumber l (**D**) with $|m| \leq l$. (**B, E**) The corresponding PSD of a random realization of the background, generated by solving the spectral space version of Eq. (1) as an l-dependent Ornstein–Uhlenbeck process (Supporting Information S1), and having the same sample size and sample rate as in (**A, D**). For comparison, black contours mark the analytic PSD given by Eq. (4), highlighting uncertainty associated with finite sampling. (**C, F**) The foreground is estimated by means of the log-scaled ratio of observed to background PSD, and is shown only where it is significantly different from 1 (Supporting Information S1). Black triangles in panel (**F**) indicate dispersion relations of gravity waves with phase speeds between 10 and 100 m s^{-1}. Black rectangles in panels (**C, F**) indicate satellite artifacts.

not necessarily imply that the foreground has zero variance, since the background and raw data are generally correlated. More waves excite more natural variability, and vice versa. Therefore, it is the power distribution in spectral space, not the total power, that distinguishes the two. In addition, it is often assumed that the foreground consists only of enhanced variability, but we argue that suppressed variability is just as important. In other words, the background has a red spectrum by definition, a first-order process in time and a second-order process in space, and the foreground consists of fluctuations whose spectrum deviates from that of the red background.

Having estimated the model parameters, we generate a random realization of the background (Fig. 4B,E) by solving the spectral space version of Eq. (1) as an l-dependent Ornstein–Uhlenbeck process (Supporting Information S1), having the same sample size and sample rate as the observed OLR. The advantage of this approach is that the realized background accounts for the effects of finite sampling, therefore providing a better basis for comparison than the analytic PSD (black contours) given by Eq. (4). The foreground (Fig. 4C,F) is then estimated as the ratio between the observed and realized PSDs, shown only where it is significantly different from one (see Supporting Information S1 for the statistical analysis). With the logarithmic scaling of the power, the foreground in panel C (F) is simply the difference between the spectra in panels A and B (D and E).

The resulting foreground is dominated by the main energy drivers of the large-scale atmosphere on subannual time scales, including planetary Rossby waves, baroclinic Rossby waves, and synoptic-scale weather. For reference, the black triangles in Fig. 4F consist of the dispersion relations of gravity waves with phase speeds between 10 and 100 m s^{-1}. The regions enclosed by these triangles are consistent with (stable) baroclinic Rossby waves with spatial scales between 2,500-4,000 km (wavenumbers between 10-16) and periods of 2-14 days (closer inspection of the origin confirms that the enhanced/suppressed variability in these regions does not extend to period longer than about 14 days). The

asymmetry between the eastward and westward propagating waves, with the former having enhanced variability, compared to the background, and the latter suppressed variability, is consistent with Doppler shifting by the mean flow (which is absent from the background). The fact that their dispersion relation matches that of gravity waves is further consistent with the fact that their scale is much larger than the Rossby deformation radius.

The side lobes of suppressed variability are consistent with unstable baroclinic Rossby waves, or synoptic weather, with spatial scales between 1000-2500 km (wavenumbers between 16-40) and periods of 2-14 days. The fact that they appear as suppressed variability is consistent with the fact that they are unstable, and therefore in shortage compared to the background. In other words, in the absence of mean flow, they are stable modes of the background. Moreover, the fact that they are symmetric with respect to eastward/westward variability is further consistent with the fact that the growth rate of unstable modes is typically larger than their frequency (the imaginary part of the phase speed is larger than its real part).

Finally, the central lobe is consistent with planetary Rossby waves with spatial scales between 5000-10,000 km (wavenumbers between 4-8) and periods of 2-14 days. They appear as suppressed variability since, in contrast to baroclinic Rossby waves, which feed on the mean flow, planetary Rossby waves feed into the mean flow and are therefore in shortage compared to the background. In addition, the central lobe likely includes the regions of suppressed variability at the poles and spectral leakage from the El Niño-Southern Oscillation, both of which project mostly on wavenumbers 0-3 (Fig. 1).

5 Conclusions and Discussion

We find that the Earth's Infrared Background (EIB) can be described as isotropic, random fluctuations implied by the fluctuation-dissipation theorem (FDT). It is generated in response to internal variability of the atmosphere on small spatiotemporal scales,

and is sustained by the Earth's energy balance at the top of the atmosphere. In particular, a simple stochastically forced energy balance climate model is capable of explaining the observed space/time spectra on subannual time scales. The resulting (joint) space-time spectrum of the background captures the total observed variance by construction, and is distributed in space and time according to a red noise process, allowing one to separate atmospheric variability of interest from the background.

Although grounded in the fundamental principle of the FDT, further work remains. The forcing and damping terms were chosen for simplicity and empirical agreement, rather than derived from first principles. The question is then what are the relevant physical processes at play. Considering the estimated (de)correlation scales, while allowing sufficient separation between the forcing and the response, and considering also the assumption that the background is isotropic, the most plausible origin of the former is instabilities associated with small-scale atmospheric turbulence. Indeed, small-scale damping is often heuristically associated with turbulent diffusion, while large-scale (synoptic) damping is associated with varying non-linear processes (Holton & Colton, 1972; Sardeshmukh & Held, 1984; Lin et al., 2008; Romps, 2014; Shamir et al., 2023). As such, this description of the background is complementary to the turbulent-centric description of the Tropical Background in Hottovy and Stechmann (2015), with an additional constraint on the scale-dependence of the forcing. A related question is what determines the (de)correlation scales of the background. We hypothesize that they are constrained by the linear wave dynamics, namely, the Rossby radius of deformation and the characteristic Rossby wave frequency.

Data Availability Statement

NOAA Interpolated Outgoing Longwave Radiation data provided by the NOAA PSL, Boulder, Colorado, USA, is publicly available on their website at https://psl.noaa.gov/data/gridded/data.olrcdr.interp.html.

The code to reproduce the analysis and figures is available at

Conflict of Interest declaration

The authors declare there are no conflicts of interest for this manuscript.

Acknowledgments

O. S. and E. P. G. were supported by Schmidt Sciences LLC. E. P. G. was also supported by the National Science Foundation through award OAC-2004572. We also acknowledge high-performance computing support from the Derecho system (doi:10.5065/qx9a-pg09) and the Cheyenne system (doi:10.5065/D6RX99HX) provided by the National Center for Atmospheric Research (NCAR), sponsored by the National Science Foundation.

References

Ardanuy, P. E., & Kyle, H. L. (1986). El Nino and outgoing longwave radiation: Observations from Nimbus-7 ERB. *Monthly weather review*, *114*(2), 415–433.

Arguez, A., & Vose, R. S. (2011). The definition of the standard WMO climate normal: The key to deriving alternative climate normals. *Bulletin of the American Meteorological Society*, *92*(6), 699–704.

Chelliah, M., & Arkin, P. (1992). Large-scale interannual variability of monthly outgoing longwave radiation anomalies over the global tropics. *Journal of Climate*, *5*(4), 371–389.

Chiodi, A. M., & Harrison, D. E. (2013). El Niño impacts on seasonal US atmospheric circulation, temperature, and precipitation anomalies: The OLR-event perspective. *Journal of Climate*, *26*(3), 822–837.

Fajary, F. R., Hadi, T. W., & Yoden, S. (2019). Contributing factors to spatiotemporal variations of outgoing longwave radiation (OLR) in the tropics. *Journal of Climate*, *32*(15), 4621–4640.

Frankignoul, C., & Hasselmann, K. (1977). Stochastic climate models, Part II Ap-

plication to sea-surface temperature anomalies and thermocline variability. *Tellus*, *29*(4), 289–305.

Gehne, M., & Kleeman, R. (2012). Spectral analysis of tropical atmospheric dynamical variables using a linear shallow-water modal decomposition. *Journal of the atmospheric sciences*, *69*(7), 2300–2316.

Hasselmann, K. (1976). Stochastic climate models part I. Theory. *tellus*, *28*(6), 473–485.

Hendon, H. H., & Wheeler, M. C. (2008). Some space–time spectral analyses of tropical convection and planetary-scale waves. *Journal of the atmospheric sciences*, *65*(9), 2936–2948.

Holton, J. R., & Colton, D. E. (1972). A diagnostic study of the vorticity balance at 200 mb in the tropics during the northern summer. *Journal of the Atmospheric Sciences*, *29*(6), 1124–1128.

Hottovy, S., & Stechmann, S. N. (2015). A spatiotemporal stochastic model for tropical precipitation and water vapor dynamics. *Journal of the Atmospheric Sciences*, *72*(12), 4721–4738.

Jiang, X., Adames, Á. F., Kim, D., Maloney, E. D., Lin, H., Kim, H., ... Klingaman, N. P. (2020). Fifty years of research on the Madden-Julian Oscillation: Recent progress, challenges, and perspectives. *Journal of Geophysical Research: Atmospheres*, *125*(17), e2019JD030911.

Kikuchi, K. (2014). An introduction to combined fourier–wavelet transform and its application to convectively coupled equatorial waves. *Climate dynamics*, *43*(5), 1339–1356.

Kikuchi, K., Kiladis, G. N., Dias, J., & Nasuno, T. (2018). Convectively coupled equatorial waves within the mjo during cindy/dynamo: Slow kelvin waves as building blocks. *Climate Dynamics*, *50*(11), 4211–4230.

Kim, K.-Y., & North, G. R. (1991). Surface temperature fluctuations in a stochastic climate model. *Journal of Geophysical Research: Atmospheres*, *96*(D10),

18573–18580.

Knippertz, P., Gehne, M., Kiladis, G. N., Kikuchi, K., Rasheeda Satheesh, A., Roundy, P. E., ... others (2022). The intricacies of identifying equatorial waves. *Quarterly Journal of the Royal Meteorological Society*, *148*(747), 2814–2852.

Knutson, T. R., Weickmann, K. M., & Kutzbach, J. E. (1986). Global-scale intraseasonal oscillations of outgoing longwave radiation and 250 mb zonal wind during Northern Hemisphere summer. *Monthly weather review*, *114*(3), 605–623.

Kubo, R. (1966). The fluctuation-dissipation theorem. *Reports on progress in physics*, *29*(1), 255.

Liebmann, B., & Smith, C. A. (1996). Description of a complete (interpolated) outgoing longwave radiation dataset. *Bulletin of the American Meteorological Society*, *77*(6), 1275–1277.

Lin, J., Mapes, B. E., & Han, W. (2008). What are the sources of mechanical damping in Matsuno–Gill-type models? *Journal of Climate*, *21*(2), 165–179.

Liu, C., Liao, X., Qiu, J., Yang, Y., Feng, X., Allan, R. P., ... Xu, J. (2020). Observed variability of intertropical convergence zone over 1998—2018. *Environmental Research Letters*, *15*(10), 104011.

Loeb, N. G., Wielicki, B. A., Doelling, D. R., Smith, G. L., Keyes, D. F., Kato, S., ... Wong, T. (2009). Toward optimal closure of the earth's top-of-atmosphere radiation budget. *Journal of Climate*, *22*(3), 748–766.

Marques, C. A., & Castanheira, J. M. (2018). Diagnosis of free and convectively coupled equatorial waves. *Mathematical Geosciences*, *50*(5), 585–606.

Masunaga, H., L'Ecuyer, T. S., & Kummerow, C. D. (2006). The madden–julian oscillation recorded in early observations from the tropical rainfall measuring mission (trmm). *Journal of the atmospheric sciences*, *63*(11), 2777–2794.

Milly, P. C., Betancourt, J., Falkenmark, M., Hirsch, R. M., Kundzewicz, Z. W.,

Lettenmaier, D. P., & Stouffer, R. J. (2008). Stationarity is dead: Whither water management? *Science*, *319*(5863), 573–574.

Mudelsee, M. (2010). *Climate time series analysis*. Springer.

North, G. R. (1975). Theory of energy-balance climate models. *Journal of the Atmospheric Sciences*, *32*(11), 2033–2043.

North, G. R., & Cahalan, R. F. (1981). Predictability in a solvable stochastic climate model. *Journal of Atmospheric Sciences*, *38*(3), 504–513.

North, G. R., Cahalan, R. F., & Coakley Jr, J. A. (1981). Energy balance climate models. *Reviews of Geophysics*, *19*(1), 91–121.

North, G. R., Wang, J., & Genton, M. G. (2011). Correlation models for temperature fields. *Journal of Climate*, *24*(22), 5850–5862.

Obukhov, A. M. (1947). Statistically homogeneous fields on a sphere. *Usp. Mat. Nauk*, *2*(2), 196–198.

Percival, D. B., & Walden, A. T. (1993). *Spectral analysis for physical applications*. cambridge university press.

Philander, S. G. H. (1983). El Niño southern oscillation phenomena. *Nature*, *302*(5906), 295–301.

Romps, D. M. (2014). Rayleigh damping in the free troposphere. *Journal of the Atmospheric Sciences*, *71*(2), 553–565.

Sardeshmukh, P. D., & Held, I. M. (1984). The vorticity balance in the tropical upper troposphere of a general circulation model. *Journal of the atmospheric sciences*, *41*(5), 768–778.

Schneider, T., Bischoff, T., & Haug, G. H. (2014). Migrations and dynamics of the intertropical convergence zone. *Nature*, *513*(7516), 45–53.

Shamir, O., Garfinkel, C. I., Gerber, E. P., & Paldor, N. (2023). The Matsuno–Gill model on the sphere. *Journal of Fluid Mechanics*, *964*, A32.

Shaw, T., Baldwin, M., Barnes, E. A., Caballero, R., Garfinkel, C., Hwang, Y.-T., ... others (2016). Storm track processes and the opposing influences of climate

406 change. *Nature Geoscience*, *9*(9), 656–664.

407 Timmermann, A., An, S.-I., Kug, J.-S., Jin, F.-F., Cai, W., Capotondi, A., ... oth-
408 ers (2018). El Niño–southern oscillation complexity. *Nature*, *559*(7715),
409 535–545.

410 Trenberth, K. E., Fasullo, J. T., & Kiehl, J. (2009). Earth's global energy budget.
411 *Bulletin of the american meteorological society*, *90*(3), 311–324.

412 Weickmann, K., & Khalsa, S. (1990). The shift of convection from the Indian Ocean
413 to the western Pacific Ocean during a 30–60 day oscillation. *Monthly Weather*
414 *Review*, *118*(4), 964–978.

415 Wheeler, M., & Kiladis, G. N. (1999). Convectively coupled equatorial waves: Anal-
416 ysis of clouds and temperature in the wavenumber–frequency domain. *Journal*
417 *of the Atmospheric Sciences*, *56*(3), 374–399.

418 Wheeler, M. C., & Hendon, H. H. (2004). An all-season real-time multivariate
419 MJO index: Development of an index for monitoring and prediction. *Monthly*
420 *weather review*, *132*(8), 1917–1932.

421 Wieczorek, M. A., & Meschede, M. (2018). SHTools: Tools for working with spheri-
422 cal harmonics. *Geochemistry, Geophysics, Geosystems*, *19*(8), 2574–2592.

423 Zhang, C. (2005). Madden-Julian oscillation. *Reviews of Geophysics*, *43*(2).

424 Zwanzig, R. (2001). *Nonequilibrium statistical mechanics*. Oxford university press.